# Chiro-Optoelectronic Encodable Multilevel Thin Film Electronic Elements with Active Bio-Organic Dielectric Layer

Moon Jong Han, Minkyu Kim, and Vladimir V. Tsukruk\*

School of Materials Science and Engineering, Georgia Institute of Technology, Atlanta, GA 30332, USA

\* Tel: 1-404-894-6081; e-mail: Vladimir@mse.gatech.edu

#### **Abstract**

We suggest that chiral photonic bio-enabled integrated thin film electronic elements can pave the base for next-generation optoelectronic processing, including quantum coding for encryption as well as integrated multi-level logic circuits. Despite recent advances, thin-film electronics for encryption applications with large-scale reconfigurable and multi-valued logic systems are not reported to date. Herein, highly secure optoelectronic encryption logic elements were demonstrated by facilitating humidity-sensitive helicoidal organization of chiral nematic phases of cellulose nanocrystals (CNCs) as active dielectric layer combined with printed-in organic semiconducting channels. The ionic-strength controlled tunable photonic band gap facilitates distinguishable and quantized 13-bit electric signals triggered by repetitive changes of humidity, voltage, and the polarization state of the incident light. As a proof-of-concept, the integrated circuits responding to circularly polarized light and humidity are demonstrated as unique physically unclonable functional devices with high-level logic rarely achieved. The convergence between functional nanomaterials and the multi-valued logic thin-film electronic elements can provide optoelectronic counterfeiting, imaging, and information processing with multilevel logic nodes.

KEYWORDS: circularly polarized processing; bio-organic field-effect transistors; multivalued logic systems; photonic cellulose nanocrystals; multifunctional logic electronics; bioenabled optical communications;

#### Introduction

In nature, unique structure colors appear in the skin of various living things, including beetles, birds, and fishes, mainly due to the complex hierarchical structure of organic and biological components. <sup>1,2,3</sup> Interestingly, some elements of the biological entities consist of chiral supramolecular structures, where the selective light reflection generates under different circularly polarized light (CPL).<sup>4</sup> Such unique photonic crystal structure over a large scale allows them to adjust in dynamic environments through optical communications, including adaptive appearance and camouflaging, found in the palatopods, cephalopods, crickets, or bees. <sup>5,6,7,8</sup> Cases of information exchange via linear and circular can be found in modern information technology <sup>9,10,11,12</sup> and spintronics effects. <sup>13</sup> Nature-inspired chiral architectures have been applied to smart materials and sensors to modulate stimulus-response behavior through selective light reflection and diffraction as controlled by environmental conditions such as humidity, heat, stress, current, and pH. <sup>14,15,16,17,18,19</sup> Such chiral assembled structures can be realized with crystalline TiO<sub>2</sub> microspheres, <sup>20</sup> thiol-acrylate chemistry, <sup>21</sup> and semi-interpenetrating polymer networks. <sup>22</sup>

However, most chiral structures are ineffective in converting changes of chiral nematic structures into readable output values. On the other hand, chiral materials from cellulose nanocrystals (CNCs) can be fabricated by an evaporation-induced self-assembly process with pitch length controlled by processing conditions. <sup>23,24,25,26</sup> The high density of the hydroxyl group on the surface of the CNCs can generate a mesoporous structure with channels and bonding sites that can be adjusted in accordance with the chiral nematic structure, <sup>27</sup> which can be alternately adjusted to the helical pitch induced by the stimulus, resulting in significant color modulation. Therefore, CNC films and coating techniques have been utilized as templates to develop humidity, <sup>28</sup> light, <sup>29</sup> stress, <sup>30</sup> and magnetic-responsive materials. <sup>31</sup> Adjustable helical pitches rely heavily on external stimuli, but practical implementation of device-related principles remains a significant challenge in the field.

Here, we demonstrate that a combination of the responsive active dielectric layer of chiral CNC films and opto-electrically triggered semiconducting conjugated channels encoded by circular polarization of light and relative humidity provides an executable design for accessing information that can be decoded by thin film electronic devices such as organic field-effect transistors (OFETs). In this design, discrete optoelectrical signals can be read out and triggered by the polarization state of the incident light, voltage, and humidity conditions. The individual

CNC-based bio-organic field-effect transistors (BOFETs) can be triggered by on/off gate voltage  $(V_{GS})$ , polarization states of light, and humidity conditions, resulting in quaternary logic systems operation. Finally, a high-level 13-digit system is demonstrated by introducing an integrated inverter comprising p- and n-type organic semiconductors. By converting the distinguishable optoelectrical signals to Alphabet letters, number substitution cyphers, an elaborate optical communication, even advanced cryptographic techniques are suggested, where external stimuli elevate the coded information space beyond traditional digital processing.

#### **Results and Discussion**

#### **Fabrication of Encryption Logic Dielectric Layers**

Fig. 1a–c shows an underlying fabrication process of the active dielectric element and optoelectrical device and a flow diagram of the optical communication with encrypting information based on treated CNC films (see fabrication procedure in the Experimental Section). Briefly, an indium tin oxide (ITO)-deposited glass acts, acting as the substrate and a standard gate electrode, is attached to the Petri dish. Under a controlled condition (25% relative humidity (RH) and T = 25 °C) for one day, evaporation-induced self-assembly (EISA) generates CNC films with the chiral nematic organization. The dry films were subsequently subjected to the dropping of different NaCl solutions to induce different photonic bandgaps (Fig. 1a). CNC layers show iridescence and selective reflection and transmission of CPL, owing to the intrinsic chirality of left-handed twisted supramolecular structures. Thus, LCPL is reflected, whereas RCPL is transmitted.

The disguisable photonic pattern of responsive photonic materials is realized depending on the salt concentration (right of Fig. 1a), due to the salt-induced change of helical pitch.  $^{35,36,37}$  Because CNCs and NaCl salt has contrasting water absorption abilities, the concentration of NaCl tunes the precise reflection color of NaCl-dropped CNC films, such as blue, green, and reddish coloration. The distinct photonic bandgaps tailor polarization state-dependent optoelectrical signals of BOFETs-based multi-valued logic systems (MVLS) (Fig. 1b). Overall, by combining relative humidity (H), salt concentration (S), and the wavelength (W) and polarization state (P) of

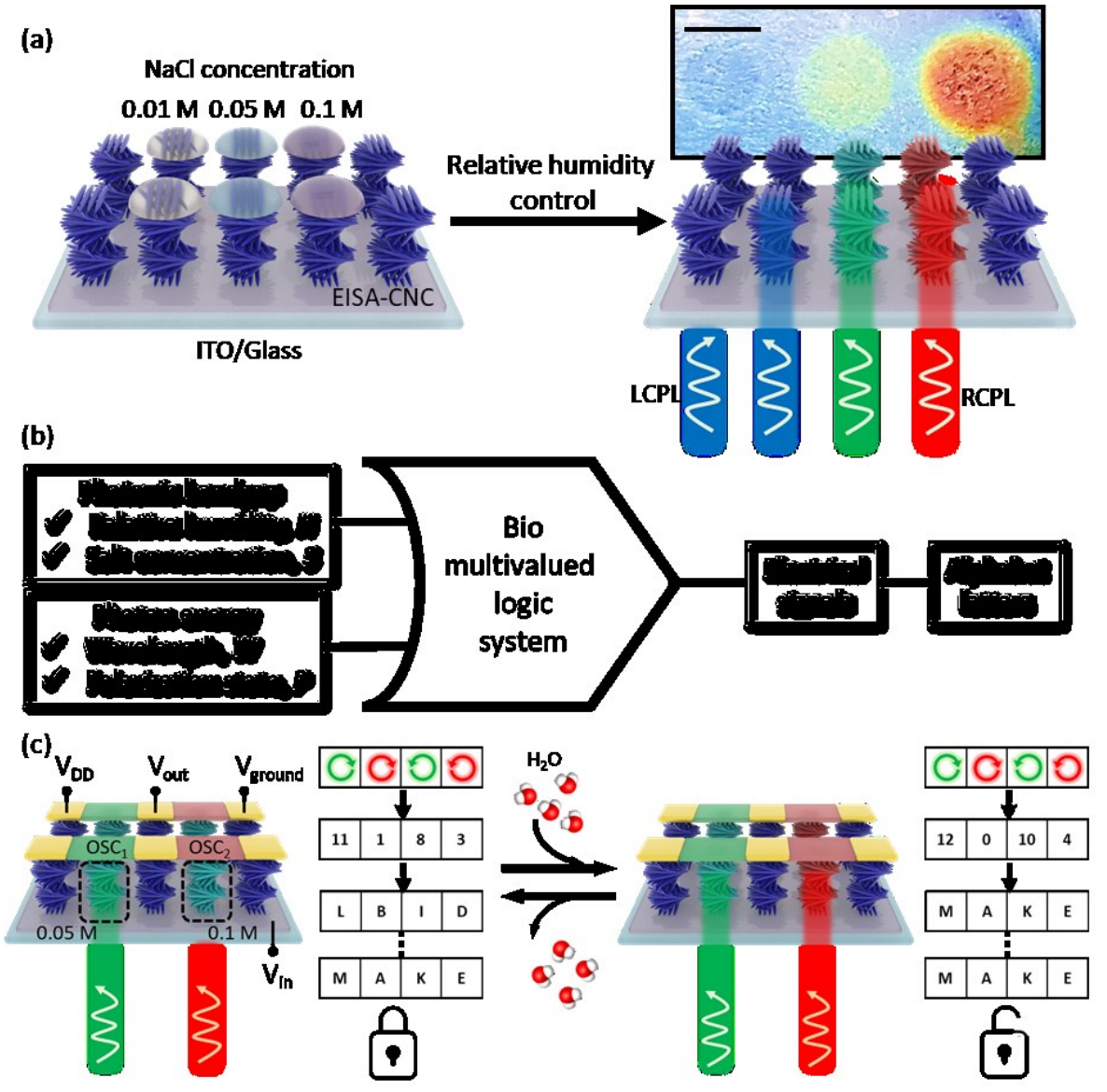


Figure 1. Multivalued logic system-based optical communication with encryption. (a) Evaporation-induced self-assembed (EISA) CNC film onto the ITO/glass substrate. By precise dropping of NaCl solutions, the chiral pitch of CNC is tuned by relative humidity control (scale bar is 1mm). (b) Graphical symbol of a bio multivalued logic system triggered by photonic bandgap (relative humidity, H and salt concentration, S) and photon energy (wavelength, W and polarization state, P), decoding electrical signals with following converted alphabet letters. (c) Optical communication based on the integrated circuits enabled active chiral bio-dielectric layers. The specific inputs afford optical communication, transiting "MAKE" signals with encryption by tuning H within the system.

the incident light - dependent chiral pitch modulation of CNC films, we design the bio multi-valued logic system (Fig. 1c). After depositing different concentration of NaCl such as 0.05 and 0.1 M onto the prepared CNC film, gold electrodes and organic semiconductors (OSCs) were patterned via thermal evaporation and ink-jet printing, respectively, to operate the integrated inverter circuits

(Fig. S1). <sup>38,39</sup> The chiral nematic organization of CNC layers reacts a distinguishable optical input to the OSCs layers and, as a result, modulates the subsequent electrical signals in the device, where the humidity-responsive chiral pitch of CNCs increases as relative humidity increases. By exposing the circularly polarized light with different wavelengths, such as RCPL (green), RCPL (red), LCPL (green), and LCPL (red), the electrical outputs are tuned and each result could be converted to a discrete value (Fig. 1c). The one-to-one matching of electrical signals and alphabet letters afford the coded optical communication and decryption. At low humidity, the resultant alphabet letters of "LBID" are switched to "MAKE" at high humidity conditions. The encoded information "MAKE" of "lock" can be unlocked when the specific inputs of the CPL and wavelengths are matched for facilitating encoded optical communication and decryption (Fig. 1c).

## Morphology and optical properties of CNC films as a dielectric layer

The atomic force microscopy (AFM) images (Fig. 2a-d) revealed the morphology of the CNC films under different salt concentrations, such as 0.05 (Fig. 2b) and 0.1 M (Fig. 2c), of the CNC films to be similar except for the 5 M case (Fig. 2d). AFM images confirm the ordered chiral nematic configuration transition to a completely segregated and disordered organization as concentration reaches 5 M. The quantitative orientational analysis of the corresponding AFM images allows for the direct evaluation of azimuthal distribution and 2D orientational parameter (Fig. S2). <sup>40</sup> Corresponding molecular orientation order parameter within microscopic surface areas is very high, 0.92, 0.91, 0.89, pristine, 0.05, 0.1 M concentration, and very low, 0.12 for 5 M, respectively. The twisted Bouligand morphology, a signature of the chiral nematic organization, of the pristine CNC at 0.1 M NaCl concentration was also confirmed by scanning electron microscopy (SEM) (Fig. 2e and Fig. S3).

CPL transmission spectra show the different CNC films show changes in photonic properties under different conditions (Fig. 2f, g), where the polarization of the incident light

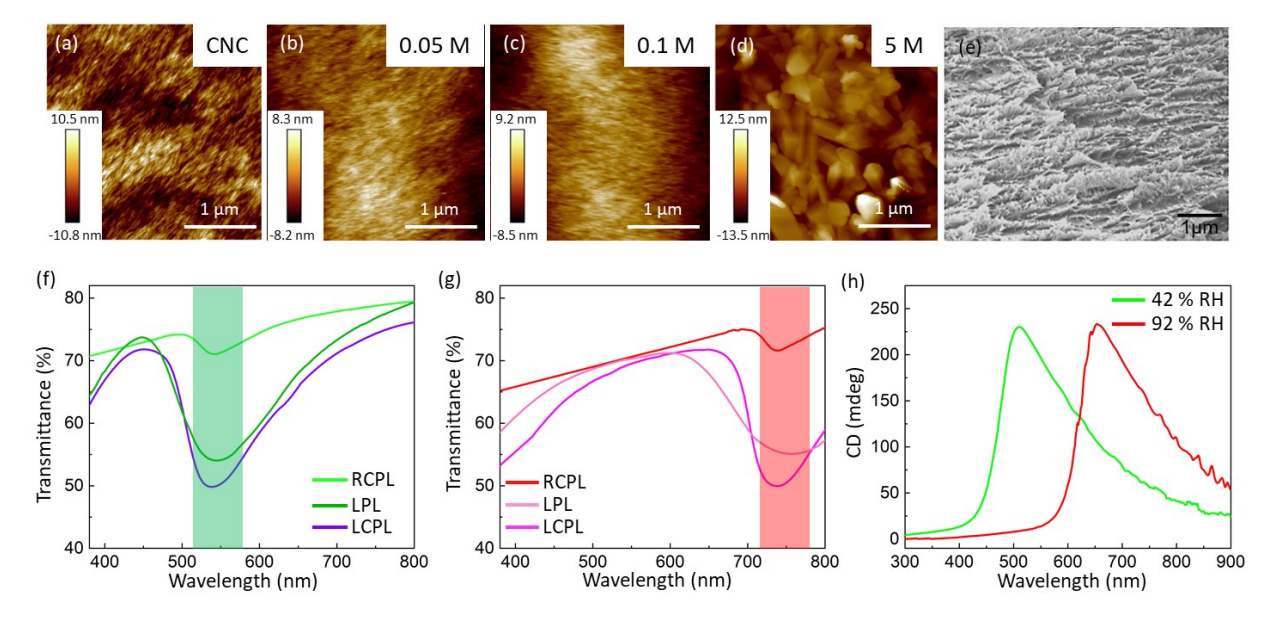


**Figure 2**. Structural characterization of active photonic CNC film with NaCl deposition. (a-d) AFM and (e) SEM image of CNC film. Especially, (b) 0.05 (c) 0.1 (d) 5 M of NaCl solution deposition onto the CNC film. UV-vis transmittance of CNC film at (f) 42 and (g) 92 % RH condition with RCPL, LPL, and LCPL polarization state. (h) CD spectra of CNC film at 42 and 92 % RH condition.

applied was left-handed circular polarized light (LCPL), linearly polarized light (LPL), and right-handed circular polarized light (RCPL) in addition to unpolarized light and dark conditions. As expected, RCPL shows an increase in transmittance in the range between 80 and 90 % with respect to the measured wavelength region. Compared with the 42 % RH condition, the salt treatment induces a change of the helical pitch with a redshift of the photonic bandgap (Fig. 2g). Linearly polarized light transmittance profile is intermediate between the RCPL and LCPL transmission (Fig. S4). The pitch length (*P*) is extracted from these spectra by using the equation (1):<sup>41,42</sup>

$$P = \frac{\lambda}{n_{avg}cos\theta} \tag{1}$$

with the peak reflection position ( $\lambda$ ), the average refractive index ( $n_{avg}$ ), and the angle between the surface normal and the incident ray ( $\theta$ ). From this equation, one can obtain the pitch length increasement with increasing RH by using an average refractive index of nanocellulose materials,  $n_{ave}=1.5.^{43}$  An increase in pitch length with humidity indicates the gradual swelling of the films by steady water adsorption and diffusion into CNC porous matrix from about 353 nm at 42% to 480 nm at 92 % RH. Therefore, it is calculated that a thickness change of approximately 40% occurs based on the wavelength change of selective reflection. It has been experimentally demonstrated that the average refractive index of CNC/NaCl is maintained identically at the

condition that humidity is changed.<sup>44</sup> Besides, the previous study experimentally measured that ~40% thickness increase of CNC/NaCl composite with RH change from 42% to 92%,<sup>44</sup> which is consistent with our result achieved from optical measurement. Furthermore, the CNC films with helical chiral nematic organization show characteristic positive peaks at circular dichroism (CD) spectra with a distinct red shift at higher humidity from 520 nm to 700 nm (Fig. 2h),<sup>45,46</sup> indicating preservation of left-handed chirality of self-assembled CNC structures at all humidity conditions.

## Individual BOFET element for photonic bandgap-controlled logic

To realize the discrete optoelectrical signal output element based on the active bio-chiral dielectric layer discussed above, the p-and n-type organic semiconductors (OSCs), PBTTT-C14 and ITIC-F, respectively, were printed for the individual BOFET element as patterned channels (Fig. S5). These compounds exhibit different strong absorption peaks around 550 and 740 nm, respectively, guaranteeing independent integrated circuits operation (Fig. S6).

The ink-jet deposited OSC channels show low surface roughness,  $R_q$  of  $2.0 \sim 2.9$  nm (1×1  $\mu m^2$  surface area), and very fine, nanoscale (< 50 nm) grain dimensions with a thickness of  $\sim 55$  nm (Fig. S7). Thus, they are capable of effective responses under the incident lights without light losses, therefore, affording efficient multi-stimuli responsive active channels (Fig. 1c).

The humidity-controlled changes in light transmittance within the BOFET element control chiro-opto-electrical signal under variable conditions (Fig. 3a, b). For low RH conditions, corresponding to the greenish reflection color's chiral pitch (Fig. 3a), the transmittance of the incident green light (550 nm LED) increases in the LCPL, LPL, and RCPL sequence. Humidity increases result in reddish coloration, tuning the negligible transmittance of three polarization states of the incident light (Fig. 3b).

Depending on the RH and the subsequent chiral pitch of CNC films, the transmittance of the different polarized lights tunes the chiro-opto-electrical outputs of the individual BOFET elements (Fig. 3c, d). Based on the p-type OSC properties of PBTTT-C14, the transfer curves (drain current vs gate voltage) clearly reveal the dramatic change in drain current for different light conditions (Fig. 3c, d). At the same time, it adjusts the transmitted light through the CNC films, directly affecting the resultant meaningful light intensities to the OSC channels. Each LED wavelength is 550 (green) and 730 nm (red), matching the absorbance bands of PBTTT-C14 and

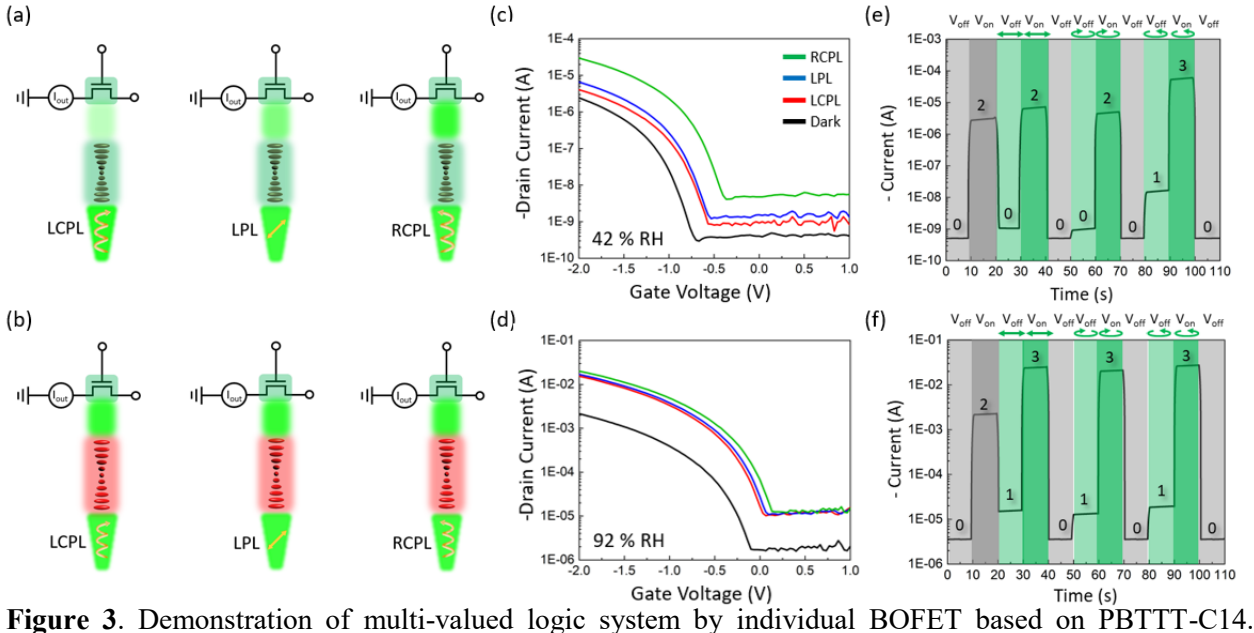


**Figure 3**. Demonstration of multi-valued logic system by individual BOFET based on PBTTT-C14. Modulation of the incident light through CNC film by varying polarization state at (a) 42 and (b) 92 % RH. (c) Transfer characterization of BOFET at (c) 42 and (d) 92 % RH, triggered by polarization state. Transient response of quaternary logic system by voltage, RH and polarization of light at (e) 42 and (f) 92 % RH.

ITIC-F, respectively. By switching the polarization state in the order of dark, LCPL, LPL, and RCPL, the high transmittance of light triggers different electrical signal outputs (Fig. 3c, d), generating high photo-generated charges within the OSC channel. The reversible electrical characterization by switching humidity from 42 to 92 % RH and vice versa (Fig. S8), where there were negligible electrical changes derived from the reversible water molecules' absorption and desorption in the system as reversible reflection color's switching.<sup>33</sup> The higher effective light intensity through the higher transmitted photonic CNC layer by tuning the polarization condition, the more shifts of the threshold voltage ( $V_{th}$ ) to the negative and positive directions, opposite for ITIC-F and PBTTT-C14 conditions, respectively, with the significant  $|I_{DS}|$  output increase. For the higher RH conditions, the negligible transmittance difference affords a similar transfer characterization by tuning the incident polarization conditions, where an increase of on-current generates, resulting from the high accumulated charges at the OSC/CNC interface (Fig. S9).

The humidity/polarization responsive behavior facilitates quaternary logic behavior (Fig. 3e, f). The transient responses of on/off  $V_{GS}$  ( $V_{on} = -2V$  and  $V_{off} = 1$  V) and under light with different polarization conditions with 10 s intervals is investigated (Fig. 3e, f). For low RH condition (Fig. 3e), 42 % RH, due to the tuned effective transmittance intensity of light, the currents are modulated depending on the polarization state of light. The logic "0", "1", "2", and

"3" correspond to each chiro-opto-electrical condition as long as the current outputs don't exceed 1 order. At higher humidity (Fig. 3f), the overall currents increase compared with low RH conditions and show negligible differences regardless of the incident light polarization states, inducing the same "3" logic value in the system.

For the ITIC-F layer (Fig. S10), the 730 nm LED modulates the chiro-opto-electrical signals with the independent RH conditions. Due to the polarization-dependent effective transmittance intensity of 730 nm light through the chiral photonic CNC layer, the opposite results are demonstrated. For low RH case, the same "2" logic value appears regardless of the polarization conditions; however, the "3" logic state generates for high RH cases under LPL and LCPL conditions. Observed changes in drain current span a very wide range from 0.5 nA to 100  $\mu$ A and from 50  $\mu$ A to 50 mA at low and high humidity, respectively (Fig. 3e, f).

The chiroptical functionality of the individual BOFET based on PBTTT-C14 is evaluated quantitatively by using a dissymmetry factor of responsivity ( $g_R$ ) according to equation:<sup>47</sup>

$$g_{R} = \frac{2(R_{RCPL} - R_{LCPL})}{R_{RCPL} + R_{LCPL}},$$

where  $R_{RCPL}$  and  $R_{LCPL}$  indicate the responsivities under the RCPL and LCPL exposure, respectively. The average  $g_R$  values were extracted to be + 1.63 and 0.52, depending on 42 and 92 % RH conditions, respectively, which is comparable to the value of the previously reported chiroptical electronics. The  $g_R$  of the ITIC-F BOFETs fabricated here was + 0.26 and 1.52 for 42 and 92 % RH conditions, respectively.

For the performance stability evaluation, the BOFETs are measured under bias stress as a function of RH, such as 42 and 92 % RH, and light irradiation of RCPL (Fig. S9). The normalized drain current ( $I_{DS}(t)/I_{DS}(0)$ ) of the time-dependent variation is explored, where  $I_{DS}(t)$  is the drain current at time t and  $I_{DS}(0)$  is the drain current at t = 0. The bias stress is constant with  $V_{GS} = V_{DS} = -2 \text{ V}$  for 1 h at different RH conditions. The normal decay of  $I_{DS}$  is measured under both 42 and 92 % RH conditions. As the concentration of water molecules at the OSC/dielectric layer interface increases, the strength of the local field also increases, and the dipoles are polarized must faster, resulting in the highly sensitive and fast decay of  $I_{DS}$  related to the field-induced charge trapping or oxygen vacancies at the semiconductor/dielectric layer interface. <sup>50,51</sup> In detail, at the highest

humidity of 92 % RH,  $I_{DS}$  decreased by 33 % within 3000 s and maintained a constant level in the remaining time of the bias stress application.

The RH dependency of the optoelectrical properties is based on both charge trapping and dielectric polarization in the FETs.<sup>52,53</sup> As RH increases, weaker charge trapping and stronger polarization cause an increasing recombination rate with a shorter time reaching the equilibrium state, leading to a faster photocurrent decay and smaller saturated photocurrent (Fig. S11).<sup>54</sup> As a representative example of the optoelectrical measurement of BOFET, RCPL illumination has been applied. For the 92 % RH condition, the time-dependent *I<sub>DS</sub>* of RCPL case decreased by 24 % within 2400 s with shorter time reaching saturation region, compared to the dark condition.

## Logic nodes based on photonic energy and bandgap tuning

Note that the light transmittance through the active dielectric layers with two different OSCs can be modulated by the photonic bandgap (*H*) of the chiral photonic layer and the effective absorbed photon energy (*W*) of OSC channels with polarization state (*P*) of the incident light as well as on/off voltage (*V*) of V<sub>in</sub> (Fig. 4). The integrated inverter circuits consisting of PBTTT-C14 and ITIC-F OSC channels are demonstrated (Fig. 4a). The *H*, *E*, *P*, and *V*-dependent chiro-optoelectrical properties for the bio-multi-valued logic system (MVLS) are shown in the Fig. 4b,c. The *H* controls the transmittance of light through CNC film under applying the different *W*, generating distinct V<sub>out</sub> within the voltage transfer curves (VTC), which can be utilized for MVL applications. The inverter shifts within the VTC toward the negative V<sub>in</sub>, which is caused by photogenerated charging with an increase in conductance of each OSCs channel. For example, at 42 % RH, the 730 nm wavelength region exhibit relatively high transmittance of the incident light compared with the 550 nm region (Fig. 2f), causing increased photo-generated charges of the ITIC-F channel than those of the PBTTT-C14 channel.

By varying the conditions of the exposed LEDs, such as dark, 550, and 730 nm, the VTC moves following the positive or negative direction, respectively. We relate this phenomenon to the transition of the cross-region from the output characteristics of p-type PBTTT-C14 and n-type ITIC-F-based BOFETs along the positive direction under different W and P of the green light

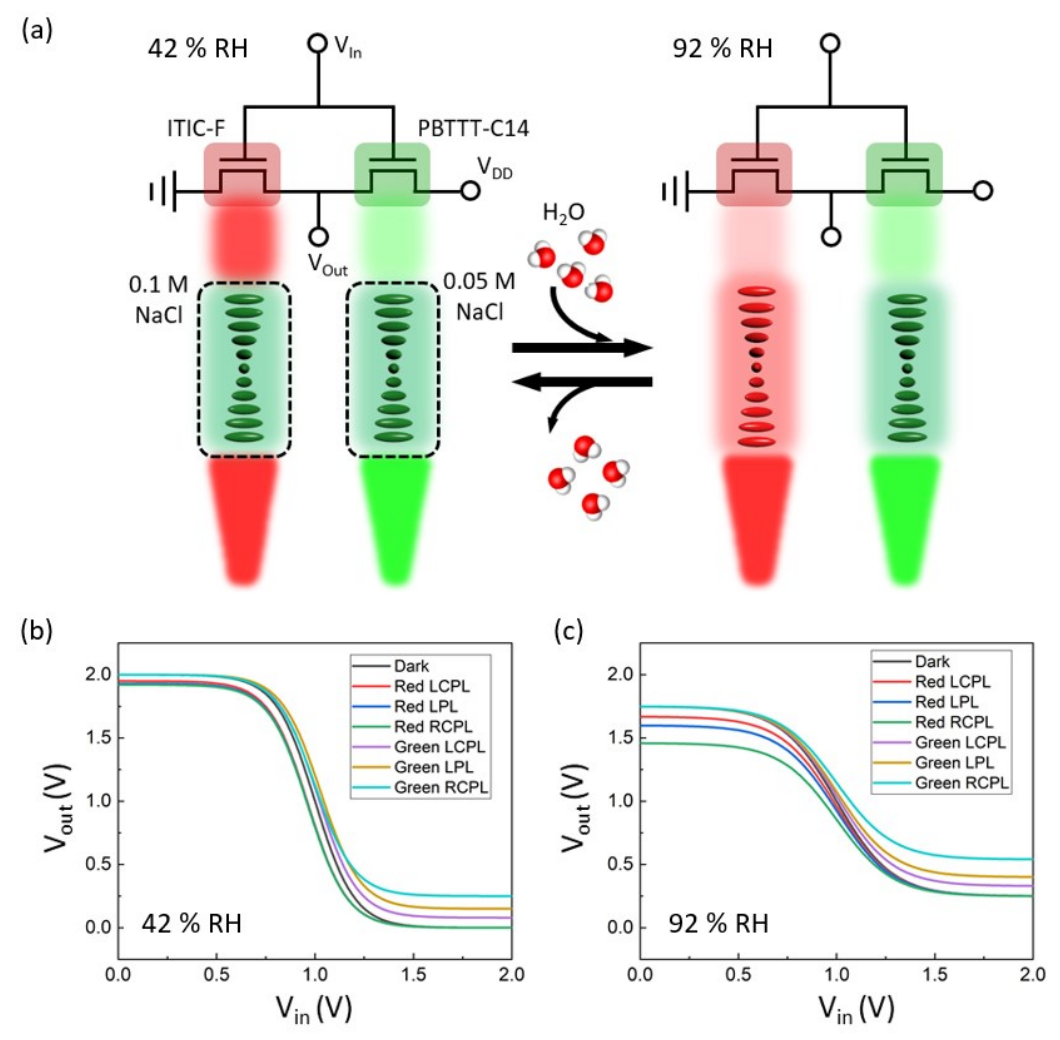


**Figure 4**. Design of 13 digit logic system based on salt concentration-dependent chiral pitch of active bio chiral dielectric layer. (a) Schematic illustration of the integrated inverter circuits triggered by salt concentration, humidity, and polarization state of the incident of light. Voltage transfer curves of the inverters at (b) low and (c) high RH condition by varying polarization of light. The active transmittance of light through CNC layer, triggered by dark, LCPL, LPL, and RCPL illumination with green and red light, tunes optoelectrical signals of the integrated inverter directly. Detailed transmittance degree follows the scheme in Fig. 3a, b.

exposure (Fig. S12). Note that the higher transmittance of green LED at low RH and red LED at high RH conditions at which an elaborate transmittance appears in the order of dark, LCPL, LPL, and RCPL (Fig. 3a, b). In the case of the red light case under 42 % RH, the transmitted light through the chiral photonic CNC layer is relatively high compared to that under the green light condition, resulting in effectively high photo-generated charges in the ITIC-F active layer. However, the negative shift of VTC happens, governed by the constant photo-induced charge mechanism. For the 92 % RH case, the V<sub>out</sub> decreases under applying low V<sub>in</sub>, resulting from the output resistance decrease with the off-current increase (Fig. 3c,d). At high V<sub>in</sub>, the V<sub>out</sub> shows a

significant increase, compared with the 42 % RH case, affected by the additional leakage current with a high concentration of water molecules. Therefore, green or red LED exposure affords the positive or negative shift within the VTC owing to the  $V_{th}$ 's positive or negative shift due to the photo charges.

Finally, the generalized reconfigurable bio-13 digit logic system is summarized in Table 1 and Fig. S13 shows the applied sequential inputs, such as H, E, E, and E are unit of the combination of three triggers corresponds to the discrete logic values of "0"  $\sim$  "12". In this system, we designate "0" corresponding to E0  $\sim$  0.05 V of V<sub>out</sub> and the other logic states were done with 0.05 V intervals (Table 1).

Inputs			Output	Inputs			0
Humidity	Optical	Electrical	Output	Humidity	Optical	Electrical	Output
Low	Dark	V <sub>out</sub>	12	Hìgh	Dark	V <sub>out</sub>	10
		V <sub>in</sub>	0			V <sub>in</sub>	3
	Green LCPL	V <sub>out</sub>	12		Green LCPL	V <sub>out</sub>	10
		V <sub>in</sub>	1			V <sub>in</sub>	4
	Red LCPL	V <sub>out</sub>	11		Red LCPL	V <sub>out</sub>	9
		V <sub>in</sub>	0			V <sub>in</sub>	3
	Green LPL	V <sub>out</sub>	12		Green LPL	V <sub>out</sub>	10
		V <sub>in</sub>	2			V <sub>in</sub>	5
	Red LPL	V <sub>out</sub>	11		Red LPL	V <sub>out</sub>	8
		V <sub>in</sub>	0			V <sub>in</sub>	3
	Green RCPL	V <sub>out</sub>	12		Green RCPL	V <sub>out</sub>	10
		V <sub>in</sub>	3			V <sub>in</sub>	6
	Red RCPL	V <sub>out</sub>	11		Red RCPL	V <sub>out</sub>	7
		V <sub>in</sub>	0			V <sub>in</sub>	3

**Table 1.** Chiro-optoelectrical outputs triggered by humidity, the polarization state of the incident light, and voltage for the configuration of Fig. 4

The efficiently absorbed light through a thin dielectric layer was confirmed by the adequate electronic device performance owing to significant light selection via the chiral nematic organization. By dropping NaCl solution (0.1 M) onto CNC films, where the pristine reflection color is red, the different chiro-optoelectrical outputs can be generated fast (Fig. S14 and Table S1). Indeed, the rate of humidity variation can be as low as 30 ms from 20 to 80 % RH if the mass flow controller and saturated aqueous solution are in use.<sup>57</sup> In terms of a system composed of a humidifier and fan motor, the humidity values can be modulated from 30 to 100% RH in 15 s.<sup>58</sup> Also, recent research demonstrated dynamic structural color-tuning characteristics based on

the cellulose composites, tuned with a relatively short response time such as a few seconds and 4 min for CNC/NaCl and CNC/polyacrylamide (PAM) case, respectively.<sup>59,60,61</sup>

## High-level 13-digit logic elements for multiplexed encrypted optical communication

Recently, we have reported the CNC composite BOFETs system, exhibiting the reconfigurable quinary logic values identically for each device array. However, to realize more subdivided logic values by facilitating the chiral supramolecular structures and salt concentration (*C*) -dependent chiral pitch modulation of the unique biopolymer characteristics, circularly polarized lights (*P*) and the solution patterning of NaCl electrolyte onto the prepared CNC film have been introduced in this study in order to design higher-level readable discrete signals. Thus, we design reconfigurable 13-digit logic values for elaborate optical communication with advanced encryption applications that were unreachable in previous designs. 62,63,64,65

For optical communication, cryptographic techniques using CPL have been suggested.  $^{66,67}$  Commonly, the telecommunication technique converts the blinking lights to digital information, where the more complex encryption is, the more amounts of flashing lights containing additional encrypted data increase. On the other hand, encrypted information by the polarized lights can be utilized as an effective technique to transform given information with no significant data amounts increase. As the polarization states of circularly polarized lights,  $\sigma_+$  and  $\sigma_-$ , are modulated or vanished, the eavesdropping phenomena could appear. By utilizing an approach, such as a wireless power supply system within free space, only designated electronics can respond to the inputs. For short-distance communication between a plurality of opposing fixed devices, polarization information can be transported without waste. However, long-distance CPL communication requires constant maintenance feedback because CPL transmission through curved optic fibers generates unreliable depolarization.

Here, a proof-of-concept dynamic encryption for optical multiplexing communication is proposed by utilizing a reconfigurable 13-digit logic system (Fig. 5). For the CNC films-based BOFET elements (encrypted device), the output signals are controlled by the multiple decoding conditions (keys) such as photon energy, E (or wavelength,  $\lambda$ ), and photon polarization, P, with both responses biased by controlled RH (H) (Fig. 5a). Through the number substitution cypher

from optoelectrical signals to the Alphabet, the information decryption can be generated the secure optical communication (Fig. 5b).

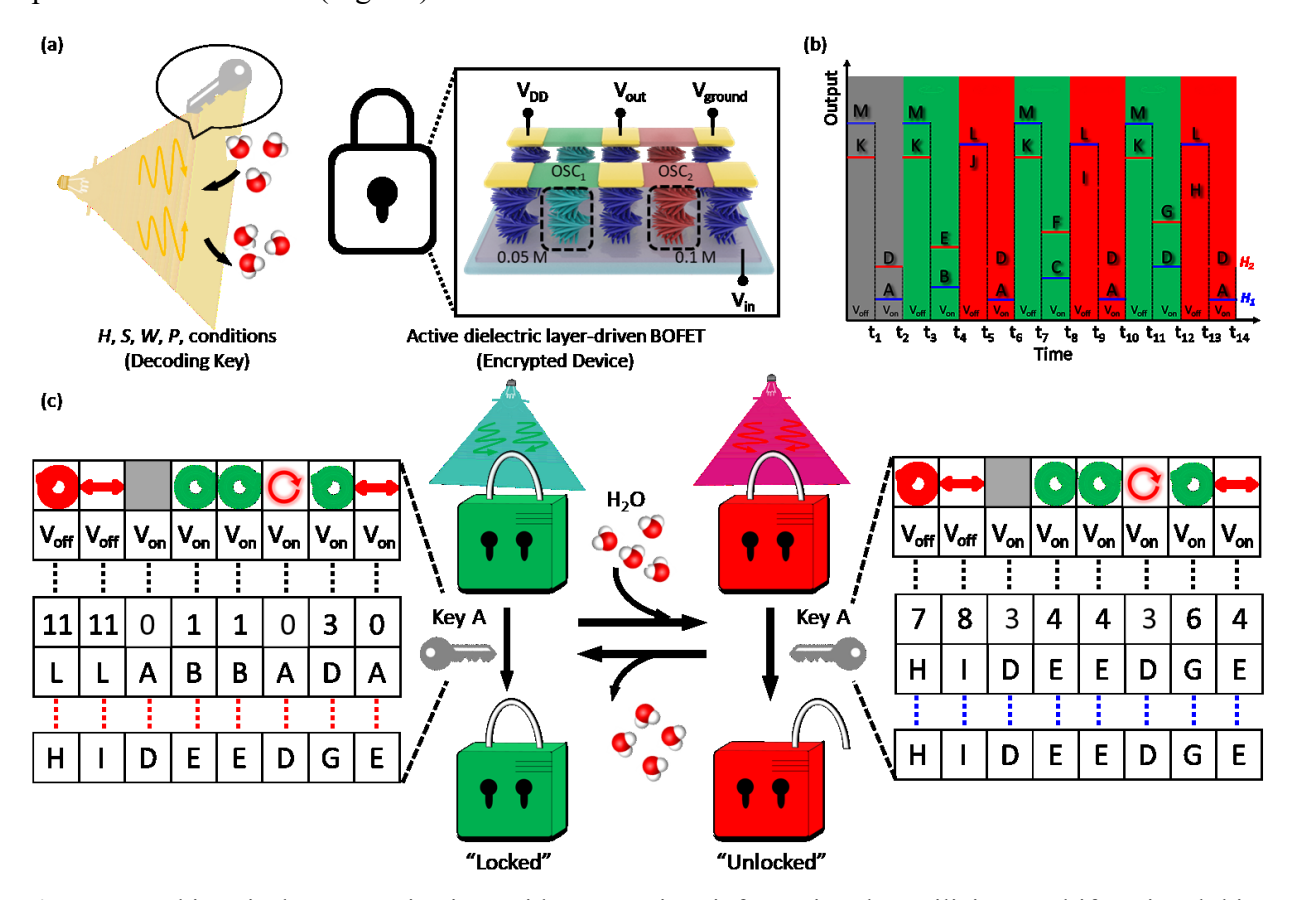


**Figure 5**. Chiroptical communication with encryption information by utilizing multifunctional biophotonic materials-based BOFETs. (a) The elements of the chiro-optoelectrical communications with encryption such as decoding keys and encrypted device. (b) Alphabet letters converted by 13 V<sub>out</sub> values by sequence. (c) Proof-of-concept of chiro-optoelectrical communication with decryption by applying chiro-optoelectrical triggers order, generating different letter sequence that decides the system unlocking.

In this design, the multiple diverse key inputs, such as polarization state, voltage, and humidity, are exploited as information transmission channels. A sequence of the polarization state of the incident light with different wavelengths, such as dark, 550, and 730 nm, is applied for low and high RH conditions. For example, RCPL, LPL, and LCPL polarization states, green and red incident lights, and on/off voltages are all explored for the dynamic encryption systems. The green and red locks represent low and high RH, respectively (Fig. 5c), being unlocked when an appropriate key matches the lock's underlying password. On the basis of the chiro-optoelectrical signals of the integrated inverters display 13-digit logic (Fig. 4), each value is transformed into the Alphabet by considering the number substitution cypher, which can express the Alphabet from "A" to "M", matching with "0" to "12" (Table S2).

This deconvolution process simultaneously transmits encrypted digital information for optical communication. The system can transmit the encrypted information and afford chiro-optoelectrical communication by detecting the lock matching with the key, which programs the photonic bandgap, absorbed photon energy of OSC layers with the polarization and on/off voltage. For example, the intended alphabetical order to be transmitted is "HIDEEDGE", but it can be transmitted by encrypting from low humidity to "LLABBADA", which can be confirmed by increasing *H* (Fig. 5). Overall, the 13- bit signals can be transmitted with only four different triggers by harnessing *H*-responsive BOFETs-based circuits, which is 7-fold more efficient than conventional single-channel optical communication at a similar readout speed.

#### **Conclusion**

In conclusion, a highly secured optoelectronic encryption methodology has been demonstrated by facilitating humidity-sensitive chiral photonic bandgap of active dielectric layer combined with light-sensitive absorption of organic conjugated channels. The consistent shift in photonic band gap can be converted into distinguishable and quantized electric signals in thin-film electronic elements by combining environmental humidity, the voltage applied, and the polarization of the incident light. For the individual BOFET element, the combined triggers can generate stable quaternary logic states by representing the drain currents, which depend on the channel type. Based on the corresponding variation in photo charging, the integrated inverter circuits show the multi-level 13-bit signal output within the voltage transfer curves, a rarely demonstrated phenomenon. The standard one-kind key encrypted system shows the weakness of comparatively low-level information protection. If the encryption and plain-text data exist simultaneously, this kind of key could be estimated by unintended invaders, and the key cannot be obtained after the decoding process. The polarization state-based encryption technique is newly developed to improve these challenges in the systems by manipulating the polarized lights, resulting in readable outputs, which provides opportunities for teleportation and dynamic encrypted systems.<sup>68,69</sup>

In the design proposed, the code complexity and its length can be easily chosen and incorporated into the visible hologram during the design process. Even if visible lights are detected, the final encoding cannot be detected without the use of the pre-programmed compensator, due to the invisible polarization states. Therefore, the conversion of discrete chiro-optoelectrical signals to

coded optical communication and decryption becomes possible. In general, by combining different physical phenomena, the novel multi-valued logic system became capable of providing the unique coding-decoding ability for prospective chiro-optoelectronic counterfeiting, image coding, and external information processing with logic nodes. The integrated inverter circuits sensing circularly polarized light and controlled humidity demonstrated here are unique physically unclonable functional device with coded optical communication and other low-power organic artificial light-induced encryption applications with highly secure optical information processing.

#### Methods

CNC Synthesis: CNCs were prepared by the sulfuric acid hydrolysis technique.<sup>70</sup> The dried wood pulp within 64 wt% sulfuric acids was stirred at 45 °C continuously. The hydrolysis process was conducted for 60 min and it was quenched by adding a tenfold volume of MiliQ Nanopure water to the solution. The diluted solution was maintained at 25 °C for 12 hr. The clear supernatant was pulled out and the precipitate was washed by centrifugation process. The resultant solution within the dialysis tube (14 kDa molecular weight cut off) was dialyzed in contrast to deionized (DI) distilled water until the pH value of DI water became constant (~ 72 hr). The DI water was changed every 3 hr for the dialysis process. The resultant solution was centrifuged at 11,000 rpm twice. Then, the collected supernatant was sonicated by a tip-sonicator (1.2 cm diameter probe, Q700 model, QSonica) for 270 s (5 s on/off with 40% amplitude).

<u>Fabrication of CNC layer:</u> The UV/Ozone treatment to the hydrophobic ITO-coated glass substrate was performed for 30 min (PSD Series, Digital UV Ozone System by NOVASCAN) to prepare the uniform spread of CNC solution. Next, the substrate was adhered by double-sided tape to the cleaned round-shaped Petri dish (diameter:  $\sim 60$  mm). The 12 mL of CNC aqueous solution (1 wt %) was poured, where chiral photonic film generates by evaporation-induced self-assembly during solvent drying for  $\sim 2$  days within a maintained condition (25% RH, T = 25 °C). Each 1 μL from 0.05, 0.1, and 5 M NaCl (Sigma Aldrich) aqueous solution was further dropped into the prepared CNC film to change the photonic bandgap.

The humidity modulation was done by putting the prepared samples into the humidity-controllable chambers. Each 42 and 92% RH, measured by a Cole-Parmer hygrometer, were prepared by a saturated solution of potassium carbonate (K<sub>2</sub>CO<sub>3</sub>) and potassium nitrate (KNO<sub>3</sub>), respectively.<sup>71</sup>

The humidity-conditioned polystyrene (2.5 cm  $\times$  2.5 cm  $\times$  2.5 cm, Ted Pella) was placed into the borosilicate glass (8  $\times$  6.5  $\times$  3 inch, MICRO), which was sealed by a parafilm with a snap lid. The prepared top glass was attached to the BOFETs substrate to keep the humidity in during electrical measurement, the prepared top glass substrate was placed onto the bottom device substrate.

Fabrication of BOFET and inverters: The poly[2,5-bis(3-tetradecylthiophen-2-yl)thieno[3,2-b]thiophene] (PBTTT-C14) (Sigma Aldrich) and 9-Bis(2-methylene-((3-(1,1-dicyanomethylene)-6,7-difluoro)-indanone))-5,5,11,11-tetrakis(4-hexylphenyl)-dithieno [2,3-d:2',3'-d']-s-indaceno[1,2-b:5,6-b']dithiophene (ITIC-F) (Sigma Aldrich) solution were prepared in chlorobenzene (Sigma Aldrich) with a 5 mg/ mL concentration. A Microfab JETLAB II was manipulated to ink-print each OSC onto the prepared CNC layer through a 40 μm diameter piezoelectric-driven inkjet nozzle, where with an accuracy of 5 μm accuracy movement based on a motorized stage. The resultant OSC channel was ~ 500 × 50 μm² with a scanning operation velocity of 1 cm/s, where the burst number of the droplets was ~50. the Au source/drain electrodes (~ 50 nm thickness) were deposited onto the CNC layers by thermal evaporation through a shadow mask under  $5.0 \times 10^{-6}$  Torr, in which length (L) and width (W) of the active channel was 500 and 50 μm, respectively. By connecting the drain and source from each p- and n-type BOFET with carbon paste, the integrated inverter circuits were demonstrated.

Optoelectrical measurement of BOFETs: The capacitance of the salt-introduced CNC layers as a function of frequency for different humidity conditions was measured by impedance spectroscopy with an LCR meter (4287A, Agilent), where a frequency range was 10 mHz to 0.1 MHz and an AC excitation voltage was 500 mV.

The BOFETs were tested under ambient RT conditions by utilizing a semiconductor parameter analyzer (4200-SCS, Keithley). For charge carrier mobilities, they were calculated by using the equation under the saturation region:

$$I_{DS} = \left(\frac{WC_i}{2L}\right) \mu (V_{GS} - V_{th})^2$$

where  $C_i$  is the geometrical capacitance value of the CNC films under different humidities. The threshold voltage  $(V_{th})$  was evaluated by a linear fitting within the linear transfer curves.

The optoelectrical characterization was performed on the dark and under LED (Thorlabs) illumination conditions ( $\sim 1 \text{ mW cm}^{-2}$ ), whose electroluminescence emission peaks were  $\sim 550$ 

and 730 nm. Before the optoelectrical experiments, the distinct exposed optical powers were evaluated by a Thorlabs 120 UV power sensor. For the real-time V<sub>out</sub> measurement of the biomultivalued logic system, different handednesses of CPL exposure were conducted by the experimental sequence of LCPL and RCPL by a rotating linear polarizer, where the rotation of the polarizer 45° clockwise from the crossed polarizer and the quarter-wave plate transmitted the RCPL and vice versa.

## Materials Characterization

For the light absorption measurement, free-standing CNC films between quartz slides were analyzed by a Shimadzu UV-3600 spectrometer with the conditioned humidity control chamber for 96 hr. To measure the response of the films to the differently polarized light, the transmission measurement was conducted by using different types of CPL filters such as LCPL, LPL, and RCPL.

CD spectroscopy of an Applied Photophysics Chirascan<sup>TM</sup>-plus was used with the prepared CNC films, where they were placed perpendicularly to the beam direction within a wavelength range  $(300 \sim 800 \text{ nm})$ .

The light tapping mode of AFM was conducted by the ICON Dimension microscope (Bruker) according to the common process. The scan rate and resolution of the evaluation were  $\sim 0.8$  Hz and  $512 \times 512$  pixels, respectively. The AFM tips (MikroMasch, HQ:XSC11/AL BS) showing a nominal tip radius of  $\sim 10$  nm with a spring constant  $\sim 2.0$  N m<sup>-1</sup> were utilized.

SEM imaging of the CNC film was performed by a Hitachi SU-8230 by introducing a 5 kV accelerating voltage. To obtain the cross-sectional image, a razor blade was utilized to cut the film and it was attached to the SEM mount side by a carbon tape. The Au layer ( $\sim 2$  nm) was deposited onto the prepared sample by using sputter technique for  $\sim 60$  s.

Optical microscopy of the reflection mode was conducted by an Olympus BX51 microscope.

## Acknowledgments

Financial support for this research is provided by National Science Foundation grant ECCS 2203806 Award, Air Force Research Laboratory grant FA8650-D-16-5404, Air Force Office for Scientific Research grant FA9550-20-1-0305, and a grant from the South Korea National Research Foundation (NRF) (MSIT:2021R1A6A3A14039290).

## **Author contributions**

M.J.H. and V.V.T. designed the research; M.J.H. conducted electronic devices measurement; M.K. synthesized and measured optical characteristics of the CNC films; M.J.H. and V.V.T. investigated the experimental results and prepared the manuscript.

## **Additional information**

The authors declare no competing financial interests.

#### References

\_

<sup>&</sup>lt;sup>1</sup> J. Zi, X. Yu, Y. Li, X. Hu, C. Xu, X. Wang, X. Liu, R. Fu. Proc. Natl. Acad. Sci. U. S. A. 2003, 100, 12576.

<sup>&</sup>lt;sup>2</sup> E. Denton, *Sci Am* **1971**, *224*, 64.

<sup>&</sup>lt;sup>3</sup> S. Vignolini, P. J. Rudall, A. V. Rowland, A. Reed, E. Moyroud, R. B. Faden, J. J. Baumberg, B. J. Glover, U. Steiner, *Proc. Natl. Acad. Sci. U.S.A.* **2012**, *109*, 15712.

<sup>&</sup>lt;sup>4</sup> R. Vaz, M. F. Frasco, M. G. F. Sales, *Nanoscale Adv.* **2020**, *2*, 5106.

<sup>&</sup>lt;sup>5</sup> T.-H. Chiou, S. Kleinlogel, T. Cronin, R. Caldwell, B. Loeffler, A. Siddiqi, A. Goldizen, J. Marshall, *Current Biology* **2008**, *18*, 429.

<sup>&</sup>lt;sup>6</sup> T. Labhart, J. Exp. Biol. **1996**, 199, 1467.

<sup>&</sup>lt;sup>7</sup> S. Rossel, R. Wehner, *Nature* **1986**, *323*, 128.

<sup>&</sup>lt;sup>8</sup> G. Horváth, *Polarized Light and Polarization Vision in Animal Sciences*, Springer-Verlag Berlin Heidelberg, Berlin **2014**, pp. 217–224.

<sup>&</sup>lt;sup>9</sup> Y. K. Takahashi, R. Medapalli, S. Kasai, J. Wang, K. Ishioka, S. H. Wee, O. Hellwig, K. Hono, E. E. Fullerton, *Phys. Rev. Appl.* **2016**, *6*, 054004.

<sup>&</sup>lt;sup>10</sup> M. Grell, M. Oda, K. S. Whitehead, A. Asimakis, D. Neher, D. D. C. Bradley, *Adv. Mater.* **2001**, *13*, 577.

J. Gilot, R. Abbel, G. Lakhwani, E. W. Meijer, A. P. H. J. Schenning, S. C. J. Meskers, Adv. Mater. 2010, 22, E131.

<sup>&</sup>lt;sup>12</sup> S. Richtberg, R. Girwidz, *Phys. Teach.* **2017**, *55*, 406.

<sup>&</sup>lt;sup>13</sup> K. Miyamoto, H. Wortelen, T. Okuda, J. Henk, M. Donath, Sci. Rep. 2018, 8, 10440.

<sup>&</sup>lt;sup>14</sup> L. W. Mi, Z. H. Guo, C. T. Liu, C. Y. Shen, *Nano Energy* **2019**, *66*, 104143.

N. Herzer, H. Guneysu, D. J. D. Davies, D. Yildirim, A. R. Vaccaro, D. J. Broer, C. W. M. Bastiaansen, A. P. H. J. Schenning, J. Am. Chem. Soc. 2012, 134, 7608.

J. E. Stumpel, E. R. Gil, A. B. Spoelstra, C. W. M. Bastiaansen, D. J. Broer, A. P. H. J. Schenning, Adv. Funct. Mater. 2015, 25, 3314.

<sup>&</sup>lt;sup>17</sup> Z. Deng, G. Zhou, L. T. Haan, *ACS Appl. Mater. Interfaces* **2019**, *11*, 36044.

<sup>&</sup>lt;sup>18</sup> Z. H. Zhang, J. W. Zhang, C. F. Cao, K. Y. Guo, L. Zhao, G. D. Zhang, J. F. Gao, L. C. Tang, *Chem. Eng. J.* **2020**, *386*, 123894.

<sup>&</sup>lt;sup>19</sup> X. W. Liu, R. Wang, T. Zhang, Y. He, J. C. Tu, X. T. Li, Sens. Actuators, B 2010, 150, 442.

<sup>&</sup>lt;sup>20</sup> S. Mohd-Noor, J. Hansol, K. Baek, Y. R. Pei, A. M. Alam, Y. H. Kim, I. S. Kim, J. H. Choy, J. Hyun, *J. Mater. Chem. A* **2019**, *7*, 10561.

<sup>&</sup>lt;sup>21</sup> W. Hu, M. Chen, Q. Wang, L. Y. Zhang, X. T. Yuan, F. W. Chen, H. Yang, *Angew. Chem., Int. Ed.* **2019**, *58*, 6698.

<sup>&</sup>lt;sup>22</sup> A. J. J. Kragt, D. J. Broer, A. P. H. J. Schenning, *Adv. Funct. Mater.* **2018**, *28*, 1704756.

<sup>&</sup>lt;sup>23</sup> K. E. Shopsowitz, H. Qi, W. Y. Hamad, M. J. Maclachlan, *Nature* **2010**, *468*, 422.

<sup>&</sup>lt;sup>24</sup> O. Kose, A. Tran, L. Lewis, W. Y. Hamad, M. J. MacLachlan, *Nat. Commun.* **2019**, *10*, 510.

<sup>&</sup>lt;sup>25</sup> R. Xiong, J. Luan, S. Kang, C. Ye, S. Singamaneni, V. V. Tsukruk, *Chem. Soc. Review*, **2020**, 49, 983.

<sup>&</sup>lt;sup>26</sup> R. Xiong, S. Yu, S. Kang, K. M. Adstedt, D. Nepal, T. J. Bunning, V. V. Tsukruk, *Adv. Mater.*, **2019**, 1905600.

<sup>&</sup>lt;sup>27</sup> B. Tardy, J. J. Richardson, L. G. G. Greca, J. L. Guo, H. Ejima, O. J. Rojas, *Adv. Mater.* **2020**, *32*, 1906886.

<sup>&</sup>lt;sup>28</sup> C. Y. Sun, D. D. Zhu, H. Y. Jia, K. Lei, Z. Zheng, X. L. Wang, ACS Appl. Mater. Interfaces **2019**, 11, 39192.

- <sup>29</sup> H. H. Chen, A. Q. Hou, C. W. Zheng, J. Tang, K. L. Xie, A. Q. Gao, ACS Appl. Mater. Interfaces 2020, 12, 24505.
- <sup>30</sup> C. Boott, A. Tran, W. Hamad, M. MacLachlan, Angew. Chem., Int. Ed. 2020, 59, 226.
- <sup>31</sup> T. X. Chen, Q. L. Zhao, X. Meng, Y. Li, H. Peng, A. K. Whittaker, S. M. Zhu, ACS Nano 2020, 14, 9440.
- <sup>32</sup> S. Kang, Y. Li, D. Bukharina, M. Kim, H. Lee, M. L. Buxton, M. J. Han, D. Nepal, T. J. Bunning, V. V. Tsukruk, *Adv. Mater.* **2021**, *33*, 2103329.
- <sup>33</sup> M. Kim, H. Lee, M. C. Krecker, D. Bukharina, D. Nepal, T. J. Bunning, V. V. Tsukruk, *Adv. Mater.* 2021, *33*, 2103674.
- <sup>34</sup> Y. Habibi, L. A. Lucia, O. J. Rojas, *Chem. Rev.* **2010**, *110*, 3479.
- <sup>35</sup> H. Wan, X. Li, L. Zhang, X. Li, P. Liu, Z. Jiang, Z.-Z. Yu, ACS Appl. Mater. Interfaces 2018, 10, 5918.
- <sup>36</sup> C. D. Edgar, D. G. Gray, *Cellulose* **2001**, *8*, 5.
- <sup>37</sup> X. M. Dong, T. Kimura, J.-F. Revol, D. G. Gray, *Langmuir* **1996**, *12*, 2076.
- T. Carey, S. Cacovich, G. Divitini, J. Ren, A. Mansouri, J. M. Kim, C. Wang, C. Ducati, R. Sordan, F. Torrisi, *Nat Commun* 2017, 8, 1202.
  X. Fang, J. Shi, X. Zhang, X. Ren, B. Lu, W. Deng, J. Jie, X. Zhang, *Adv. Funct. Mater.* 2021,
- <sup>39</sup> X. Fang, J. Shi, X. Zhang, X. Ren, B. Lu, W. Deng, J. Jie, X. Zhang, *Adv. Funct. Mater.* **2021**, 31, 2100237.
- <sup>40</sup> N. E. Persson, M. A. McBride, M. A. Grover, E. Reichmanis, *Chem. Mater.* **2016**, *29*, 3.
- <sup>41</sup> H. de Vries, *Acta Cryst* **1951**, *4*, 219.
- <sup>42</sup> P.-X. Wang, W. Y. Hamad, M. J. MacLachlan, *Nat Commun* **2016**, *7*, 11515.
- <sup>43</sup> I. Cunha, R. Barras, P. Grey, D. Gaspar, E. Fortunato, R. Martins, L. Pereira, *Adv. Funct. Mater.* **2017**, 27, 1606755.
- <sup>44</sup> T. H. Zhao, R. M. Parker, C. A. Williams, K. T. P. Lim, B. Frka-Petesic, S. Vignolini, *Adv. Funct. Mater.***2019**, *29*, 1804531.
- <sup>45</sup> M. Kim, K. Pierce, M. Krecker, D. Bukharina, K. Adstedt, D. Nepal, T. Bunning, V. V. Tsukruk, ACS Nano 2021, 15, 19418.
- <sup>46</sup> M. Kim, H. Lee, R. T. Snipes, M. J. Han, V. V. Tsukruk, *Small* **2022**, *18*, 2104340.
- <sup>47</sup> G. Albano, G. Pescitelli, L. Di Bari, Chem. Rev. **2020**, 120, 10145.
- <sup>48</sup> H. Han, Y. J. Lee, J. Kyhm, J. S. Jeong, J. H. Han, M. K. Yang, K. M. Lee, Y. Choi, T. H. Yoon, H. Ju, S. k. Ahn, J. A. Lim, *Adv. Funct. Mater.* **2020**, *30*, 2006236.
- <sup>49</sup> J. Cheng, F. Ge, Y. Xiang, H. Zhang, Y. Kuai, P. Hou, D. Zhang, L. Qiu, Q. Zhang, G. Zou, J. Mater. Chem. C 2020, 8, 6521.
- J. Lee, J.-S. Park, Y. S. Pyo, D. B. Lee, E. H. Kim, D. Stryakhilev, T. W. Kim, D. U. Jin, Y.-G. Mo, Appl. Phys. Lett. 2009, 95, 123502.
- <sup>51</sup> L.-C. Liu, J.-S. Chen, J.-S. Jeng, *Appl. Phys. Lett.* **2014**, *105*, 023509.
- <sup>52</sup> M. Qu, H. Li, R. Liu, S. L. Zhang, Z. J. Qiu, *Nat. Commun.* **2014**, *5*, 3185.
- <sup>53</sup> C. M. Aguirre, P. L. Levesque, M. Paillet, F. Lapointe, B. C. St-Antoine, P. Desjardins, R. Martel, *Adv. Mater.* **2009**, *21*, 3087.
- <sup>54</sup> K. Yang, S. Yuan, Z. Qiu, Y. Zhan, A. A. Umar, L. Zheng, F. Seoane, *Org. Electron.* **2019**, *69*, 42.
- <sup>55</sup> H. Kim, G. Kim, I. Song, J. Lee, H. Abdullah, C. Yang, J. H. Oh, *RSC Adv.* **2018**, *8*, 14747.
- <sup>56</sup> J. G. Labram, P. H. Wöbkenberg, D. D. C. Bradley, T. D. Anthopoulos, *Org. Electron.* 2010, 11, 1250.
- <sup>57</sup> J. He, P. Xiao, J. Shi, Y. Liang, W. Lu, Y. Chen, W. Wang, P. Théato, S.-W. Kuo, T. Chen, *Chem. Mater.* **2018**, *30*, 4343.
- <sup>58</sup> J.-U. Lee, Y.-W. Ma, S.-Y. Jeong, B.-S. Shin, *Micromachines* **2020**, *11*, 476.

- 63 X. Fang, H. Ren, M. Gu, Nat. Photonics **2020**, 14, 102.
- <sup>64</sup> P. Zheng, Q. Dai, Z. Li, Z. Ye, J. Xiong, H. C. Liu, G. Zheng, S. Zhang, Sci. Adv. **2021**, 7, eabg0363.
- <sup>65</sup> J. Tan, Q. Li, S. Meng, Y. Li, J. Yang, Y. Ye, Z. Tang, S. Qu, X. Ren, *Adv. Mater.* 2021, 33, 2006781.
- <sup>66</sup> C. H. Bennett, *Phys. Rev. Lett.* **1992**, *68*, 3121.
- <sup>67</sup> S. Kak, P. Verma, G. MacDonald, in (Eds.: C. Roychoudhuri, A. Yu. Khrennikov, A. F. Kracklauer), San Diego, California, USA, **2011**, p. 81210M.
- <sup>68</sup> H. Zhou, B. Sain, Y. Wang, C. Schlickriede, R. Zhao, X. Zhang, Q. Wei, X. Li, L. Huang, T. Zentgraf, ACS Nano 2020, 14, 5553.
- <sup>69</sup> J. Kim, D. Jeon, J. Seong, T. Badloe, N. Jeon, G. Kim, J. Kim, S. Baek, J.-L. Lee, J. Rho, ACS Nano 2022, 16, 3546.
- <sup>70</sup> S. Beck-Candanedo, M. Roman, D. G. Gray, *Biomacromolecules* **2005**, *6*, 1048.
- <sup>71</sup> L. Greenspan, *Sect. A* **1977**, *81A*, 89.
- <sup>72</sup> M. E. McConney, S. Singamaneni, V. V. Tsukruk, *Polymer Reviews* **2010**, *50*, 235.

<sup>&</sup>lt;sup>59</sup> Z. Li, J. Wang, Y. Xu, M. Shen, C. Duan, L. Dai, Y. Ni, Carbohydrate Polymers 2021, 270, 118385.

<sup>&</sup>lt;sup>60</sup> T. H. Zhao, R. M. Parker, C. A. Williams, K. T. P. Lim, B. Frka-Petesic, S. Vignolini, Adv. Funct. Mater. 2019, 29, 1804531.

<sup>61</sup> T. Lu, H. Pan, J. Ma, Y. Li, S. W. Bokhari, X. Jiang, S. Zhu, D. Zhang, ACS Appl. Mater. Interfaces 2017, 9, 18231.

<sup>62</sup> M. J. Han, M. Kim, V. V. Tsukruk, *ACS Nano*, **2022**, *16*, 13684.